12th International Symposium on Turbulence and Shear Flow Phenomena (TSFP12)
Osaka, Japan (Online), July 19-22, 2022

CURVATURE EFFECTS ON COMPRESSIBLE TURBULENT SHEAR LAYERS

Kristen V. Matsuno
Department of Mechanical Engineering
Stanford University
Stanford, CA 94305
kmatsuno@stanford.edu

Sanjiva K. Lele
Department of Mechanical Engineering
Department of Aeronautics & Astronautics
Stanford University
Stanford, CA 94305
lele@stanford.edu

ABSTRACT

Fundamental data representing the simultaneous effects of compressibility, density variation, and curvature as primary turbulence generation mechanisms remains sparse. This work builds off our previous suite of LES studies on the combined effects of these three variables, with a specific focus on curvature effects. Various measures of shear layer thicknesses and growth rates are presented. Exact self-similarity is not achieved, although mean field and turbulent stress profiles show reasonable collapse. Growth rates and turbulent stresses for stably and unstably curved configurations are compared, and the effects of increasing curvature intensity are presented. Lastly, a comparison with compressibility effects suggests that for the given parameter range, curvature and compressibility effects are comparable.

INTRODUCTION

Many aerospace applications involve high-speed jet plumes with complex flow physics and multiple turbulence mechanisms. A comprehensive understanding of turbulence in these flows is essential in developing and improving numerical methods for such vehicle design and analysis, and is currently lacking. In particular, the shear layers in these rocket-motor exhaust plumes exhibit streamwise curvature, along with pressure gradients, shock waves, and other complexities. Prior studies focused on turbulent mixing have been limited to compressibility and variable density effects, but studies of turbulence at combining all three turbulence mechanisms (compressibility, density variation, and curvature), has been sparse.

An area which has been particularly less studied is the joint effect of streamwise curvature and compressibility in mixing layers, although streamwise curvature effects have been considered in more detail in other flows. An analogy between the phenomena in turbulent shear flow under buoyancy and under streamwise curvature was first drawn by Bradshaw (1973), which depended on the close correlation between temperature and streamwise velocity fluctuations. Later, Castro & Bradshaw (1976) studied the non-constant curvature in impinging flow and examined Reynolds stresses along the shear layer centerline. Experimental studies of simple mixing layer configurations with streamwise curvature at moderately compressible levels have not been conducted. Plesniak *et al.* (1994) also conducted experiments of nearly incompressible, mildly curved mixing layers, and observed that shear layers grew approximately linearly and that vortical structures that developed were related to upstream disturbances rather than the Taylor-Görtler instability. Stability analysis by Otto *et al.* (1996) indicated that centrifugal instability modes in the form of longitudinal vorticies are supported in curved, incompressible mixing layers if the centerline curved into the faster stream. Experiments of reacting, curved mixing layers with a focus on scalar mixing and hydrodynamic instabilities were conducted by Karasso & Mungal (1997), where it was observed that mixing efficiency did not increase in unstable configurations. Later, curvature effects on turbulent channel flows were studied by Nagata & Kasagi (2004) with a specific focus on increasing curvature intensity on turbulence intensity. Several experimental studies of streamwise curvature effects in turbulent boundary layers have been conducted (Jeans & Johnston (1982); Wang *et al.* (2017)), but similar experiments of curved shear layers across a comparable parameter space are lacking. Aside from our prior work (Matsuno *et al.* (2022)), numerical studies of curved mixing layers in the highly compressible regime have not been conducted.

The primary goal of this work is to improve the understanding of turbulent mixing layers influenced by compressibility and curvature. Large eddy simulations (LES) of turbulent shear layers at low and high M_c, and stable and unstable curvature configurations, are analyzed to improve the current understanding of the fundamental physics behind turbulent mixing in flows with multiple physical effects. Metrics for shear layer thicknesses and growth rates, and including a discussion of their evolution for stable and unstable configurations, are presented. The effects of increasing curvature intensity on turbulent statistics are demonstrated. The analogy between centrifugal and buoyancy effects, following work by Bradshaw (1973) and Nagata & Kasagi (2004), is also evaluated. Finally, compressibility and curvature effects for the present parameter range are compared.

Table 1: Physical parameters and curvature levels during initial and turbulent 'asymptotic' growth

M_c	u_2/u_1	$\delta_\Gamma(0)/r_c$	Turb. δ_Γ/r_c	Final $\dot{\delta}_\Gamma/\Delta u(0)$	Final $\Delta u/\Delta u(0)$
0.2	0.5	0.001	0.005 - 0.008	0.071	0.98
	0.5	0.010	0.075 - 0.108	0.035	0.97
	1.9	0.001	0.004 - 0.011	0.069	1.00
	1.9	0.010	0.061 - 0.110	0.140	1.01
0.8	0.2	0.001	0.006 - 0.009	0.036	0.99
	0.2	0.005	0.022 - 0.027	0.018	0.98
	0.2	0.010	0.049 - 0.108	0.018	0.96
	4.5	0.001	0.006 - 0.009	0.025	1.01
	4.6	0.005	0.025 - 0.040	0.061	1.02
	4.8	0.010	0.056 - 0.085	0.079	1.04

FLOW CONFIGURATION

The temporally developing curved shear layer configured as two co-annular streams which are periodic in the streamwise and spanwise directions. The outer and inner radial free stream values are denoted $_1$ and $_2$, respectively, in the remainder of this paper. The initial conditions for the curved shear layer are set such that vorticity is zero everywhere except within the shear layer region.

The physical parameters governing this flow are the curvature intensity, the convective Mach number, the velocity ratio, and the density ratio across the shear layer. The curvature intensity, defined as the ratio of the (initial) shear layer thickness compared to the radius of curvature, is selected to range from $\delta_0/r_c = 0.001$ to $\delta_0/r_c = 0.01$. The convective Mach number, $M_c = \Delta u/(c_1 + c_2)$, a measure of the mean flow's compressibility, was selected to be $M_c = 0.2$ and 0.8 in order to provide comparison of compressibility and curvature effects. Nominally unity density ratio configurations $\rho_2/\rho_1 = 1$ were selected for analysis in order to focus on simple curvature effects due to kinematics, without large mean density gradient effects. For the curvature intensities investigated, centrifugal instability attributed to the velocity and compressibility of the mean flow can be considered. Eckhoff & Storesletten (1978) gave the necessary stability criterion for a compressible columnar vortex (with $u_z = 0$) as

$$\Phi = \frac{u_\theta^2}{r}\left(\frac{1}{\rho}\frac{d\rho}{dr} - \frac{u_\theta^2}{c^2 r}\right) > 0 \tag{1}$$

Eckhoff & Storesletten also demonstrated that the derivation of this expression recovers the classic Rayleigh criterion for centrifugal stability in the incompressible limit, $d(\Gamma^2)/dr > 0$. The present unity density ratio shear layers are stably curved for $u_2/u_1 < 1$, and unstably curved for $u_2/u_1 > 1$, as summarized in Table 1.

Initial conditions

Each stream in the curved shear layer is setup to be vorticity-free in the mean flow. The shear layer region is centered about the centerline radius r_c with an initial thickness of δ_0. The initial values for the constant free stream total pressure, P_t, and entropy, ξ_i, for each free stream $i = 1,2$ are set according to Eqn. 2-3. Both streams have the same ratio of specific heats, $\gamma = 1.4$, and gas constant R_g.

$$P_t(r) = P_{t,1}g + P_{t,2}(1-g) \tag{2}$$

$$\xi(r) = \xi g + \xi(1-g) \tag{3}$$

$$g(r) = \frac{1}{2}\left[1 + \tanh\left(\frac{r-r_c}{\delta_0}\right)\right]$$

The streamwise velocity profile is set by the circulation as $u_\theta = \Gamma/r$, and the pressure profile is computed by integrating $dp/dr = \rho u_\theta^2/r$ from $r = r_c$ to the upper and lower boundaries, using a reference pressure p_{ref} at the centerline. This reference pressure is set such that the speed of sound at the centerline is a constant c_{ref} for all cases. The initial conditions satisfy potential, inviscid flow. To induce turbulence, solenoidal velocity perturbations were added to the shear layer. By selecting simple profiles for each u'_θ and u'_r, the remaining spanwise component of the fluctuating velocity can be solved analytically from the continuity equation to maintain a divergence-free initialization. For u'_θ and u'_r, sinusoidal perturbations are added at selected spatial modes $k_\theta^{(i)} = i2\pi/L_\theta$ and $k_z^{(j)} = j2\pi/L_z$ for $i, j \in [4,8]$ with amplitude $A(r) = exp[\sigma(r-r_c)^2]$. These perturbations decay exponentially with a rate of $\sigma = 5$ into the free streams. The initial perturbation amplitude is $0.05\Delta\bar{u}$ and phases ϕ were chosen randomly for each mode. The chosen form for velocity perturbations is given below.

$$u'_\theta = \sum_{i,j} A(r)\cos(k_\theta^{(i)}\theta + \phi_1)\cos(k_z^{(j)}z + \phi_2)$$

$$u'_r = \sum_{i,j} A(r)\sin(k_\theta^{(i)}\theta + \phi_1)\sin(k_z^{(j)}z + \phi_2)$$

$$u'_z = \sum_{i,j} \frac{A(r)}{rk_z^{(j)}}\sin(k_\theta^{(i)}\theta + \phi_1)[(1-2r(r-r_c))\cos(k_z^{(j)}z + \phi_2) + k_\theta^{(i)}\sin(k_z^{(j)}z + \phi_2)]$$

NUMERICAL METHODS

The high-resolution LES have been generated with the CFD solver OVERFLOW. Convective fluxes are computed with WENO5 and 4^{th} order Runge-Kutta time integration. In the mixing layer region, the grid has uniform and isotropic grid spacing with more than 30 points across the initial shear layer. For the inner and outer radial free streams, upper and lower 'buffer' regions with grid stretching were applied. The upper and lower boundaries of the domain are adiabatic slips walls which enforce zero radial velocity at the wall. Buffer regions in the form of grid stretching and numerical dissipation were also implemented; further details on the LES calculations are given in our previous documentation (Matsuno *et al.*, 2022).

RESULTS

Growth rates

Notation and coordinates used throughout the remainder of this work are the centerline radius r_c, the centerline streamwise position $s = r_c\theta$, and the normalized transverse coordinate $\eta = (r-r_c)/\delta_{99}$. The 99% thickness, δ_{99}, is based off the mass-averaged circulation profile, $\tilde{\Gamma} = r\tilde{u}_\theta$, and is similar to the visual thickness reported by previous experimental studies of planar shear layers. Another thickness defined from the mean circulation, which is constant in each of the free streams, can be computed. Equation 4 defines this 'circulation' thickness, δ_Γ, which is analogous to the definition of momentum

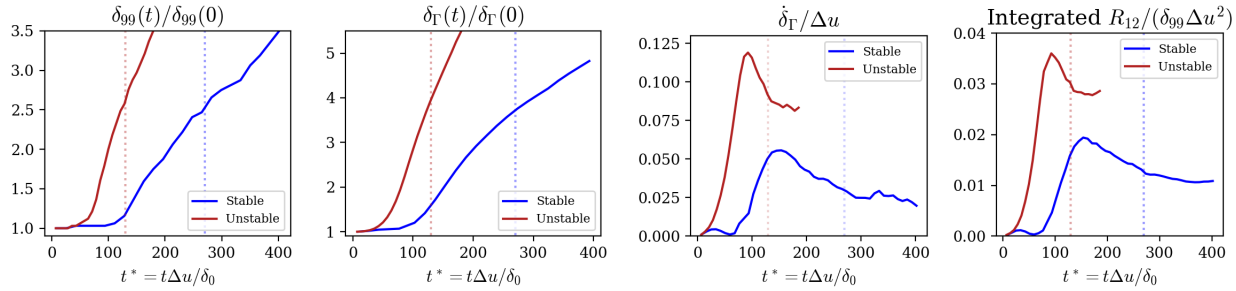

Figure 1: Thickness and growth rate measures for stable and unstable cases at $M_c = 0.8$ and $\delta_0/r_c = 0.01$.

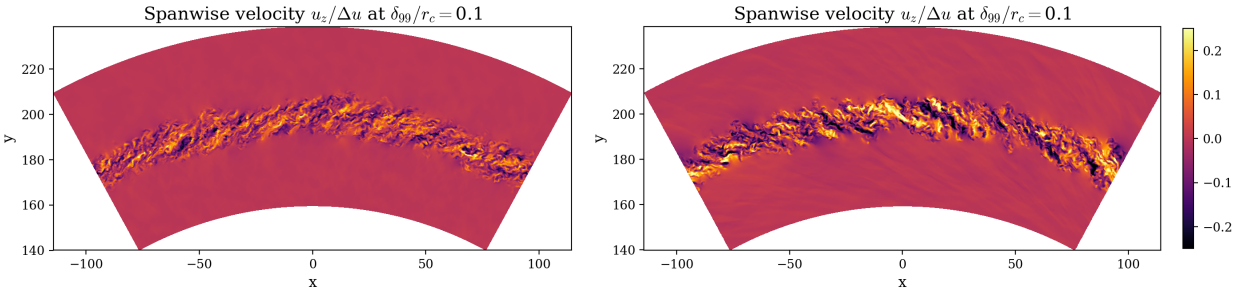

Figure 2: Spanwise velocity fields of stable (left) and unstable (right) cases for $M_c = 0.8$ and $\delta_0/r_c = 0.01$. The domain has been truncated in the radial extent for visualization purposes.

thickness for planar shear layers.

$$\delta_\Gamma(t) = \frac{1}{\rho_0(\Delta\Gamma)^2}\int_{R_2}^{R_1} \bar{\rho}(\Gamma_1 - \tilde{\Gamma})(\tilde{\Gamma} - \Gamma_2)dr \qquad (4)$$

An expression for the growth rate based off the circulation thickness can be defined by taking the time derivative of Eqn. 4[1]. This analysis follows a similar derivation of planar shear layer growth rate by Vreman *et al.*, where the integrand is first expanded and rewritten in terms of the mean momentum and kinetic energy equations. The explicit expression used to compute an integral growth rate, neglecting viscous effects, is given below, where $K = \frac{1}{2}\tilde{u}_\theta^2$, and $R_{12} = \widetilde{u_\theta'' u_r''}$.

$$\frac{d\delta_\Gamma}{dt} = \frac{2}{\rho_0(\Delta\Gamma)^2}\int_{R_2}^{R_1}\left[r\frac{\partial}{\partial r}(r\bar{\rho}\tilde{u}_r K + r\tilde{u}_\theta\bar{\rho}R_{12}) - r^2\bar{\rho}R_{12}\frac{\partial\tilde{u}_\theta}{\partial r} + r^2\tilde{u}_r\frac{\partial\bar{p}}{\partial r}\right]dr$$

Various measures of shear layer evolution are shown in Fig. 1. The left-most figure shows the evolution of the 99% thickness for two high speed shear layers at $M_c = 0.8$ with stabilizing and destabilizing curvature. After a period of transient growth, the flow becomes turbulent once the shear layer has growth to approximately twice its initial δ_{99} thickness. This occurs around a normalized convective time of $t^* = 100$ for the unstable case, and $t^* = 240$ for the stable layer. While the transient growth phase is not a focus of this study, it has been consistently observed that the more stable configurations require a longer transitional period before turbulence begins. Compared to the plot of δ_{99}, the evolution of the circulation thickness is a much smoother due to its integral form. Both time histories of the shear layer thickness definitions are normalized by the initial value and predict the same trend in growth rates with respect to curvature, namely that the destabilizing configuration results in a growth rate four times larger than the stable configuration.

The growth of the circulation thickness normalized by the initial velocity difference, $\dot{\delta}_\Gamma/\Delta u$, indicates approximately three periods of adjustment in the shear layer evolution. First, a period of transient perturbation growth occurs, corresponding to the peaks in growth rates at $t^* = 80$ for the unstable case and $t^* = 140$ for the stable case. The second period is a transition to well-developed turbulence, between $t^* \in [80, 130]$ for the unstable case and $t^* = [150, 270]$ for the stable case. A similar evolution can be seen for the shear stress integrated across the shear layer, when normalized by the instantaneous thickness $\delta_{99}\Delta u^2$. The distinction between this second transitional period and the asymptotic growth period is not clearly defined, but have been estimated based off these plots. The corresponding start times with respect to the shear layer evolution have been marked with transparent dotted lines in Fig. 1. The curvature ratios δ_Γ/r_c during the periods chosen for collection of statistics are given in Table 1. In this work, cases are referred to by their initial curvature levels. However, the overall change in curvature intensity seen by the turbulent shear layer are more moderate. For example, while the approximately planar configuration has an initial curvature of 0.001, its final curvature intensity as measured by δ_Γ/r_c approaches that of the intermediate curvature cases. Lastly, Table 1 also presents the final growth rate normalized by the initial velocity difference for each case. These tabulated rates are not exactly constant, but represent the final turbulent growth rate measured before eddies begin to be constrained by the computational domain.

Stable vs. unstable configuration

Unstable and stable configurations at $\delta(0)/r_c = 0.01$ and $M_c = 0.8$ will be compared in this section. The velocity ratio

[1]Note: Our previous derivation of this growth rate erroneously excluded terms from this integrand; the equation for integrated growth rate is corrected here.

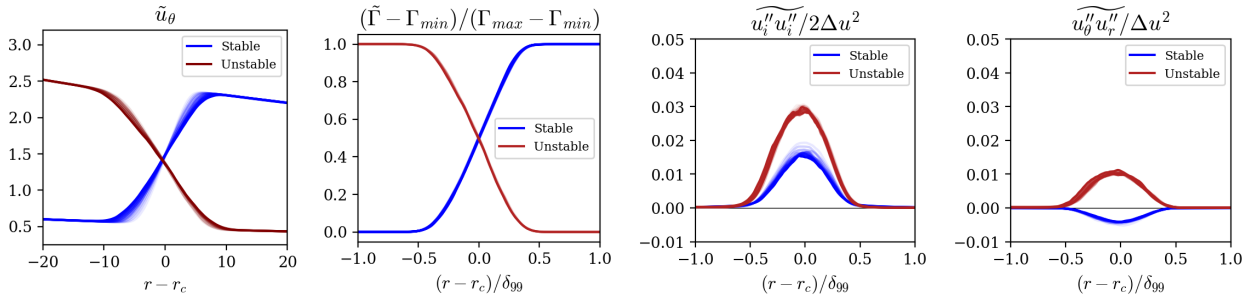

Figure 3: Mean profiles of stable and unstable configurations at $M_c = 0.8$ and $\delta_0/r_c = 0.01$.

is reciprocal between the stable and unstable cases, while the velocity difference Δu is initially the same[2]. Differences in shear layer evolution can clearly be seen in Fig. 1. Transition to turbulence and development into an asymptotically growing turbulent state occurs about twice as quickly for the unstable case compared to the stable case. Even during the peak growth period of the stable shear layer, the growth rate remains less than the growth rate of the planar shear layer.

Instantaneous spanwise velocity fields for the two configurations are shown in Fig. 2. In all configurations, this azimuthal flow travels in the clockwise direction. Two distinct differences between the turbulence in the two configurations can be easily observed by comparing these two visualizations. The magnitude of turbulent fluctuations in the unstable case is larger than that of the stable case (both plots use the same color scale). This difference in turbulent stresses can also be seen in the profiles of TKE in Fig. 4. The peak TKE in the unstable case is nearly twice that of the stable case. Note that the striation along the shear layer is opposite for the stable and unstable cases; this direction of shearing for the turbulent eddies is consistent with the streamwise velocity gradient in the two cases. In the stable configurations, the streamwise velocity u_θ is higher along the outer free stream; and in the unstable configurations, u_θ is higher along the inner free stream. The corresponding evolution of mean velocity profiles during multiple snapshots during turbulent growth are plotted by radius r in Fig. 3 (a) to show spreading of the shear layer. There is a small, negative velocity gradient in each of the free stream regions in order to ensure that the free streams have constant circulation and do not introduce vorticity to the mixing layer. Note that this requires the velocity difference across the shear layer to also change as the shear layer spreads, though the change is relatively small (see Table 1). For the stable cases, Δu decreases in time, whereas it increases in time for the unstable cases. In planar shear layers, Δu remains constant and the mean shear decreases as the shear layer grows. In the stable configuration, because the velocity difference decreases as the shear layer grows, the mean shear contributing to TKE production and eddy growth are further reduced.

The mean circulation for these same profiles are plotted by $(r - r_c)/\delta_{99}$ in Fig. 3 (b) to show approximate similarity during a subset of the turbulent period. Likewise, collapsed profiles of TKE and turbulent shear stress R_{12}, normalized by the instantaneous velocity difference, are also compared. For both the stable and unstable cases, the peak R_{12} magnitude is consistently one third of the TKE magnitude. The shear stress is positive in the unstable case and negative in the stable case, which is consistent considering the production of shear stress is dependent on the mean velocity gradient.

[2]In a temporally developing, planar shear layer the growth rate depends on the velocity difference, and not the free stream velocity ratio.

Effects of increasing curvature intensity

The effects of increasing curvature for both stabilizing and destabilizing curvature are shown in Fig. 4. The growth rate for the stable case with intermediate curvature, $\delta_0/r_c = 0.005$, is lower than previously anticipated, and the final growth rate approaches the final growth rate of the higher curvature case. A similar trend of closeness between TKE and shear stress magnitude can be seen between theses two cases as well. An explanation for this unexpected trend in the stably curved cases remains to be determined.

The curvature intensity appears to influence the transient periods of the stable and unstable growth rates, such that cases with intermediate curvature levels of $\delta_0/r_c = 0.005$ have a thickness growth which is mostly bounded by the lower and higher curvature cases. The asymptotic growth periods between the stable and unstable configurations show some notable differences. The unstable configurations appear to reach their asymptotic growth period more quickly compared to the stable configurations. These periods of growth correspond to the regions where the integrated shear stress also begin to plateau. In contrast, the stabilizing configurations did not exhibit any region of growth which was definitively linear. The upper left two plots in Fig. 4 instead show that the δ_Γ in the stable cases have progressively slower growth rates which continue to drift until the computational domain is exceeded. Normalized TKE and shear stress profiles for the unstable cases have distinct magnitudes, with the intermediate curvature case sitting evenly between the low and higher curvature cases. In contrast, the difference in TKE and shear stress magnitudes for the stabilizing curvature cases is less evenly distributed. Consistent with the observed growth rates, the cases with initially higher curvature have similar magnitudes of TKE and shear stress which are distinct from the low curvature case.

If the turbulence in curved free shear layers is considered similar to that in boundary layer flow along a concave or convex surface, structural differences in the mixing layer may be expected. In particular, the presence of Görtler vorticies or other spanwise-coherent structures may be expected to form in the turbulent region. While some qualitative differences can be observed in the mixing layer's spanwise organization while perturbations grow into turbulence, a clear difference coherent structures was not observed when the flow becamee fully turbulent. This observation remained unaffected by compressibility levels. At both low and high speeds, during periods of well-developed turbulent growth, large-scale spanwise vorticies were not seen in the mixing region.

Small differences can be observed in instantaneous snapshots of streamwise vorticity for unstable configurations, as shown in Fig. 5. These snapshots are shown for comparable times during the shear layer evolution ($\delta_{99}(t)/\delta_{99}(0) = 1.6$). A low curvature levels, the vortical region is compact and nearly uniform in height across the span of the mixing layer.

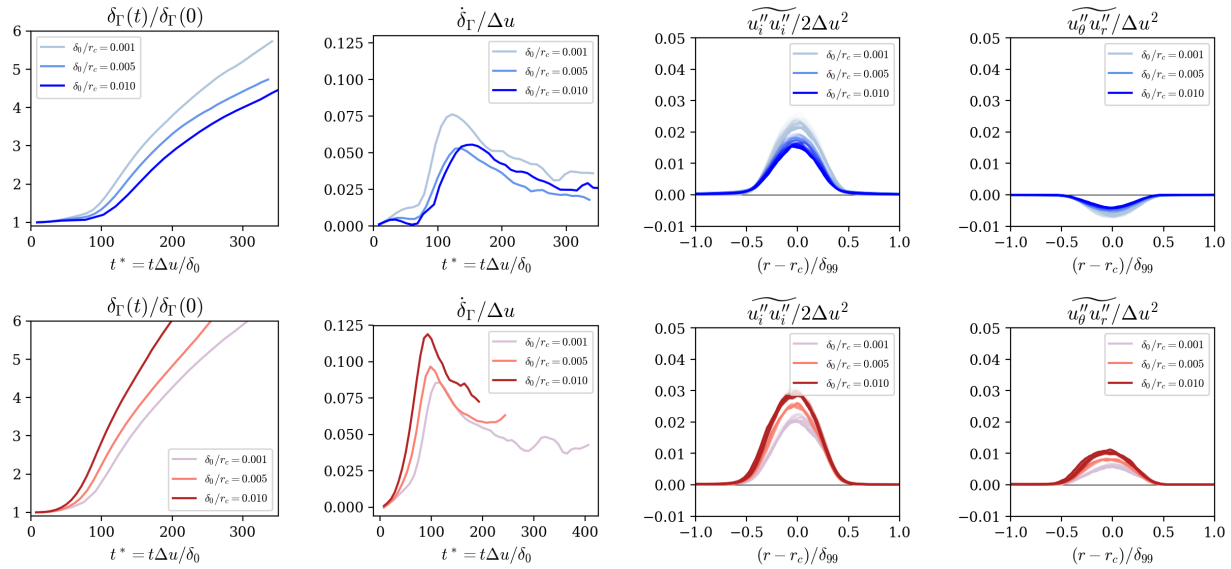

Figure 4: Evolution of thicknesses, growth rates, TKE, and R_{12} for stable (top) and unstable (bottom) cases at $M_c = 0.8$.

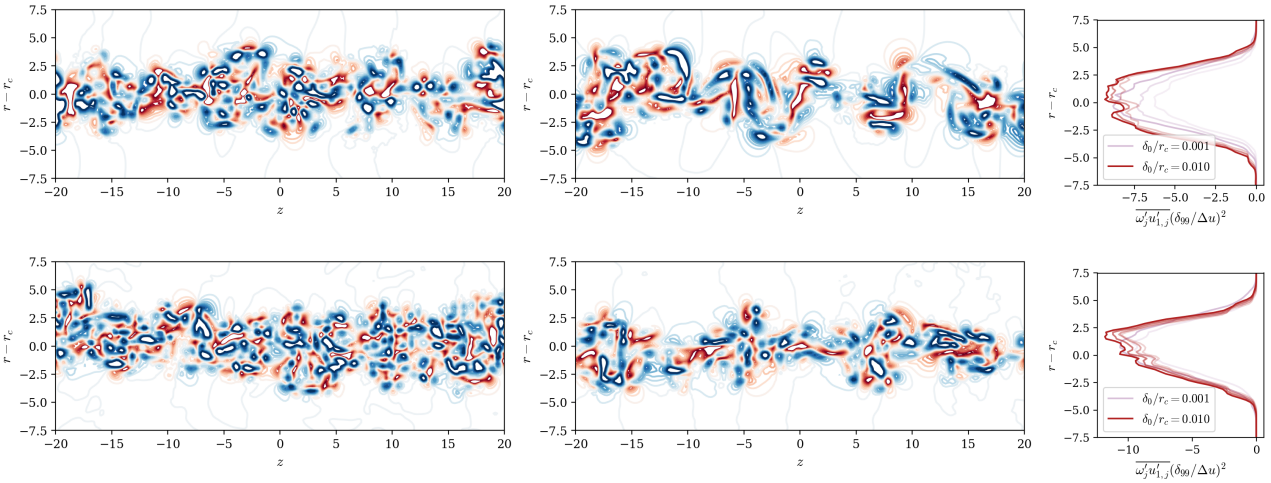

Figure 5: Instantaneous normalized streamwise vorticity at contour levels $\omega_\theta \delta_{99}/\Delta u \in [-5, 5]$ along a spanwise $(r - z)$ plane for unstable cases and rofiles of streamwise vortex stretching. The domain has been truncated for visualization purposes. Top: $M_c = 0.2$ at $\delta_0/r_c = 0.001$ (left) and $\delta_0/r_c = 0.01$ (right). Bottom: $M_c = 0.8$ at $\delta_0/r_c = 0.001$ (left) and $\delta_0/r_c = 0.01$ (right).

At higher curvature levels, a less compact region of vorticity is observed in the mixing region. In addition this sparsity, slight stretching of streamwise vorticity can be observed from the anisotropy of contour levels. This effect is more obvious for the low speed cases, where elongated iso-contours of vorticity are seen. The right-most profiles in Fig. 5 show the turbulent vortex stretching term of the mean streamwise vorticity transport equation, $\overline{\omega_j' u_{i,j}'}$, normalized by the instantaneous scales. Three profiles at times leading up to the visualization time are plotted to indicate the drift in value during this transient period. Statistical noise is evident in the profiles, but a general form of the vortex stretching profile can be gleaned. As seen qualitatively in the instantaneous visualizations, the normalized stretching of streamwise vorticity is slightly amplified for increased curvature intensity. The intermittent vorticity field also suggests that higher levels of curvature achieve equivalent shear layer thicknesses over a shorter development period.

These visualizations are shown to highlight the differences in the vortical structures during early shear layer evolution. However, as the turbulence developed further, larger vortical structures or roll cells were not observed. Profiles of streamwise velocity fluctuations, u_θ'', during the time period of fully developed turbulence ($\delta_{99}(t)/\delta_{99}(0) = 3$) are shown in Fig. 7. Streaks of elongated streamwise coherence are visible, but definite differences in the organization of u_θ'' were not observed. The apparent lack of large-scale spanwise structure in the fully turbulent regime is similar to experimental observations by Jeans & Johnston (1982) for incompressible turbulent boundary layers under concave curvature. Experiments by Wang *et al.* (2017) showed clusters of spanwise vorticity and swirl in supersonic boundary layers under convex curvature, but the clusters' spanwise extent was not shown.

Regions of sparse vorticity may be expected as the shear layer 'falls apart' during the early evolution of unstable cases, compared to stable cases with a restoring force of the free stream pressure gradient. In stable cases, due to the velocity ratio $u_2/u_1 < 1$, the free stream pressure gradient in the radial direction which scales as $dp/dr \sim u^2/r$ is largest along the outer free stream. As a result, it is possible that vorticies which may otherwise stray into the outer free stream flow from the

main mixing region are pushed back by the increasing mean pressure further from the mixing layer. The parameter governing this balance between shear and centrifugal production can be written similarly to a flux Richardson number R_f for stratified flow. As discussed in detail by Bradshaw (1973) and later revisited by Nagata & Kasagi (2004), an analogous R_f for centrifugal flows can be written considering the production of turbulent stresses $R_{\theta\theta}$ and R_{rr}. Taking the first term of $P_{\theta\theta}$ as the shear production term and $R_{12}\tilde{u}_\theta/r$ as the centrifugal production term of $P_{\theta\theta}$ and P_{rr}, the balance between shear and centrifugal terms is given in Eqn. 5.

$$P_{\theta\theta} = -2R_{12}\frac{\partial}{\partial r}\left(\frac{\tilde{u}_\theta}{r}\right) - 4R_{12}\frac{\tilde{u}_\theta}{r} \qquad P_{rr} = 4R_{12}\frac{\tilde{u}_\theta}{r}$$
$$R_f = 2\tilde{u}_\theta \Big/ r^2\frac{\partial}{\partial r}\left(\frac{\tilde{u}_\theta}{r}\right) \tag{5}$$

Profiles of R_f for stable and unstable flows, plotted with solid lines in Fig. 6, indicate increasing curvature for unstable flows gives a more negative value of R_f in the mixing layer and increasing curvature for stable flows gives a more positive value of R_f, especially near the mixing layer edges. For the stable cases, the velocity gradient includes two zero-crossings which cause the discontinuity in R_f near the mixing layer edges. Both the stable and unstable configurations give $R_f \approx -1$ in the free streams, which implies the two terms in the $R_{\theta\theta}$ production cancel and the TKE production is zero. Thus, this definition of R_f confirms that the free streams are stable. The parameter for Eckhoff's stability criterion, Φ as defined in Eqn. 1, is also plotted with dashed lines in Fig. 6 to demonstrate the centrifugal stability of the curved shear layer is dependent only on the shear layer region and not on the free stream behavior.

Comparison to compressibility effects

The effect of compressibility in planar shear layers is a four- to five-fold suppression of growth rate between incompressible and highly compressible shear layers (Papamoschou & Roshko (1988)). For the M_c range in this work, which varies from quasi-incompressible at $M_c = 0.2$ to moderately compressible at $M_c = 0.8$, the data shows $\geq 50\%$ decrease in growth rates. As given in Table 1, at low, stabilizing curvatures, the growth rate reduction is 0.036/0.071 = 0.507. At higher, destabilizing curvatures, the growth rate reduction is 0.079/0.14 = 0.564. In comparison, the difference in growth rate $\delta_\Gamma/\Delta u$ between the most stable and the most unstable cases gives a factor of four difference at both $M_c = 0.8$ and

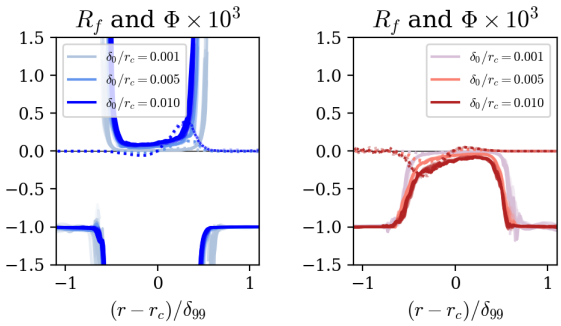

Figure 6: Profiles of R_f (solid lines) and Φ (dashed lines) for high speed stable (left) and unstable (right) cases with increasing curvature intensity.

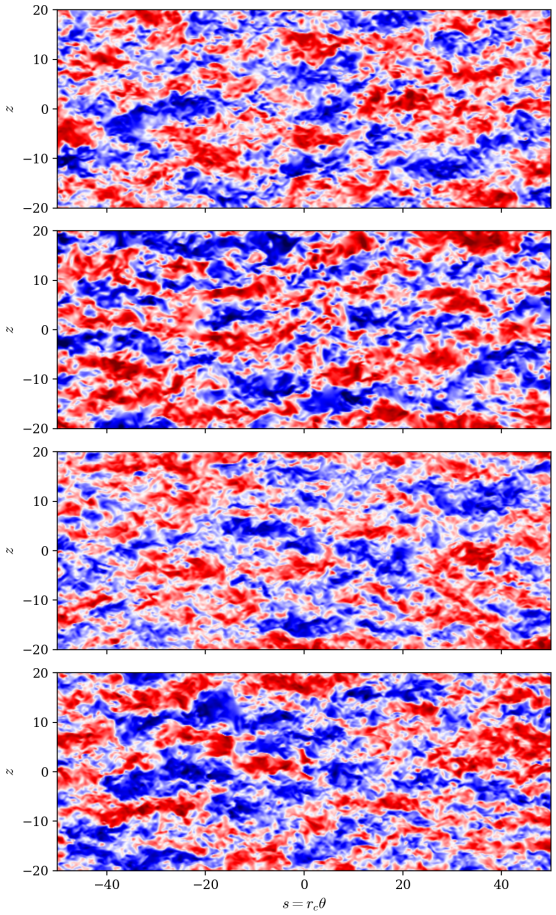

Figure 7: Instantaneous visualizations of normalized streamwise velocity fluctuations at contour levels $u''_\theta/\Delta u \in [-0.5, 0.5]$ along a streamwise $(\theta - z)$ plane for centrifugally unstable cases. The streamwise extent has been truncated by 50% for visualization purposes.

$M_c = 0.2$. In the present data, the compressibility effect remains relevant across the ranges of curvature intensities explored. The trends observed suggest that, for the given range of curvature intensities, the effects of stabilizing and destabilizing curvature may be just as important as compressibility effects.

CONCLUSIONS & FUTURE WORK

This work augments our prior investigation of turbulence in curved, compressible shear layers. Two shear layer thicknesses based on the mean circulation profile are used and thickness growth rates for stable and unstable cases are presented. While a period of turbulent stress collapse exists, the flow is not perfectly self similar. Increasing curvature intensity increases turbulent kinetic energy and shear stress for unstably curved cases, and slightly decreases the stress magnitudes for stably curved cases. An analogous 'flux' Richardson number is evaluated and defines the stability of the flow consistent with Eckhoff's and Rayleigh's centrifugal stability criteria. DNS calculations of the spatially developing equivalent of this temporal shear layer are in progress.

REFERENCES

Bradshaw, P. 1973 The effect of streamline curvature on turbulent flow. In *ADARGDograph 169*.

Castro, IP & Bradshaw, P 1976 The turbulence structure of a highly curved mixing layer. *J. Fluid Mechanics* **73** (2), 265–304.

Eckhoff, K & Storesletten, L 1978 A note on the stability of steady inviscid helical gas flows. *J. Fluid Mechanics* **89** (3), 401–411.

Jeans, AH & Johnston, JP 1982 The effects of streamwise concave curvature on turbulent boundary layer structure. *Tech. Rep.*. MIT., Cambridge.

Karasso, PS & Mungal, MG 1997 Mixing and reaction in curved liquid shear layers. *J. Fluid Mechanics* **334**, 381–409.

Matsuno, K, Lele, S & Childs, R 2022 Curvature, variable density and compressibility effects in turbulent shear layers (6.2022-0055). In *AIAA SciTech 2022 Forum*.

Nagata, M. & Kasagi, N. 2004 Spatio-temporal evolution of coherent vortices in wall turbulence with streamwise curvature. *J. Turbulence* **5** (1), 017.

Otto, S., Jackson, T. & Hu, F. 1996 On the spatial evolution of centrifugal instabilities within curved incompressible mixing layers. *J. Fluid Mechanics* **315**, 85–103.

Papamoschou, D. & Roshko, A. 1988 The compressible turbulent shear layer: an experimental study. *J. Fluid Mechanics* **197**, 453–477.

Plesniak, M., Mehta, R. & Johnston, J. 1994 Curved two-stream turbulent mixing layers: Three-dimensional structure and streamwise evolution. *J. Fluid Mechanics* **270**, 1–50.

Vreman, A., Sandham, N. & Luo, K. 1996 Compressible mixing layer growth rate and turbulence characteristics. *J. Fluid Mechanics* **320**, 235–258.

Wang, Q., Wang, Z. & Zhao, Y. 2017 The impact of streamwise convex curvature on the supersonic turbulent boundary layer. *Physics of Fluids* **29** (11), 116106.